Hindawi
Advances in Civil Engineering
Volume 2020, Article ID 8864074, 12 pages
https://doi.org/10.1155/2020/8864074

Research Article

Research of Transitional Failure Mode as Damage Evolution in Rock Wall

Xiao-guang Li,[1,2] Changhong Li,[1] Yuan Li,[1] and Pu-jin Zhang[3]

[1]*Department of Civil Engineering, University of Science and Technology Beijing, Beijing 100083, China*
[2]*Dongcheng District Committee of the Communist Youth League, Beijing 100007, China*
[3]*China Tiejian Real Estate Group Co., Ltd., Beijing 100039, China*

Correspondence should be addressed to Yuan Li; sbfqp@126.com

Received 13 May 2020; Revised 3 August 2020; Accepted 14 August 2020; Published 7 September 2020

Academic Editor: Guoqing Cai

The stress condition of tunnel surrounding rock mass is complex. The stress concentration of in situ brittle rock mass caused by excavation results in localized damage evolution parallel to the free face, which is called surface instability. The rock wall shows the transition characteristics of the failure mode with the distance from the surface to the depth. Low strength surface instability and transition failure modes of the tunnel's rock wall are common in deep condition but cylindrical specimens cannot simulate stress state of rock wall surface well in conventional rock mechanics tests. This paper conducted the indoor experimental study of the biaxial stress state and studied the surface instability of samples. An indoor test device for the simulation of transitional surface failure of the rock wall was developed. Through a biaxial stress loading test on the rectangular rock sample, the damage process and crack development of rock samples were analyzed, and the law of stress and strain related to the failure mode transition was characterized as well. Based on test results and strength analysis, an explanation of the failure theory and its corresponding model are proposed based on the maximum strain strength theory. Furthermore, this paper concludes that the failure mode of surface instability presents transition feature from brittle to ductile with the increase of distance from the surface to depth.

1. Introduction

With the construction of tunnel engineering, petroleum industry, and disposal tunnel of nuclear wastes in the past 40 years, the deformation and failure characteristics of deep brittle hard rocks have been extensively investigated and studied. Excavation in deep hard rock causes a sudden release of high intensity energy stored in the rock mass, which plays an important role in inducing surface spalling and rock burst [1–3]. It has been widely accepted that the spalling and rock burst near the surface of rock wall is a typical brittle failure [4, 5]. W. f. Brace et al. studied the entire process of brittle-shear fracture under compression and proposed that the failure process of brittle rock can be divided into the following stages [6, 7]: fracture closure, linear elastic deformation, fracture initiation, stable fracture propagation, fracture coalescence, development of unstable fractures, failure, and fracture mode after peak strength. The initial stress (σ_{ci}) and fracture damaging stress (σ_{cd}) can be determined according to the stress-strain relationship of uniaxial compression test. The failure of deep-buried brittle hard rock is an unconventional brittle failure that has the dual mechanism of brittle failure and shear failure. Recent research has mainly focused on the brittle-shear properties of high-stress rock mass. Hoek–Brown proposed that the brittle rock mass will transform into the ductility when enough confining pressure is applied [8]. Hoek–Brown failure criterion provides an acceptable estimate of the peak strength for shear failure but a cutoff has been added for tensile conditions. However, the criterion does not adequately explain the progressive coalition of tensile cracks and the final shearing of the specimens at higher confining stress [9]. Parterson conducted experiments on the marble at room temperature and proved that the rock deformation behavior changed from brittleness to ductility with the

increase of pressure [7]. Mogi has published similar experimental results and pointed out that the brittle-to-ductile transformation is usually related to rock strength [10]. On the other hand, some studies have shown that the overall strength of the rock increases with the increase of depth, and the rock becomes more brittle along with the increasing depth, which has been verified in the field monitoring of the Mine by experimental tunnel and the deep underground laboratory at Auspar [11]. Rock mass damage at great depths near underground openings is often of shear-tensile failure character [12]. To further study the failure mode transformation of the surrounding rock along the vertical inward direction of the chamber wall and the tensile failure of the rock wall and to simulate the bidirectional stress state of the chamber, a chamber wall failure simulation instrument was developed to study the transitional failure mode of the rock wall [13]. Maximum principal strain theory and maximum shear stress theory are two failure strength theories which are often used in the failure analysis of rock and rock mass. The difference between them is failure mode which is controlled by extensional strain or shear stress. Barton and Shen [14] mentioned that many scholars pointed out that the importance of axial splitting in response to the compressive stress fields, when neighbouring surfaces were available to allow the "lateral" extensional strain to cause extensional fracturing. Stacey [15] showed that, for a material that showed linear deformation behaviour, the onset of failure and the depth of failure could be related to a consideration of extensional strain. Based on the failure features analysis, the maximum principal strain formula is proposed for the initiation of surface instability calculation in this paper.

2. Test Methods for the Transitional Failure Simulator of the Rock Wall

2.1. Manufacture of the Sample Chamber. Referring to the design idea of the surface instability instrument developed by Kao [16], to consider the geometric factors (plane shape) and the biaxial stress state of the surrounding rock surface of tunnel, techniques such as endoscopy laser speckle technology, LVDT technology, digital image technology, and acoustic emission technology are utilized to measure and locate the internal and external deformation of the specimens. Compared with the traditional triaxial test, rock wall surface damage is progressive; this would be involved in the research on the transformation of failure mode and the geometric factors [17]. Meanwhile, the axis displacement, surface displacement, internal displacement, cracking signal, pressure data, and other relevant information require to be obtained. Furthermore, a servo loading test should be carried out to simulate the stable failure process of the surface rock of deep tunnel, which is in cooperation with a lateral displacement-control technique. The instrument is presented in Figure 1.

To ensure the measurement accuracy, the LVDT sensor was calibrated to obtain a linear range of around 5 mm, which was used as the measurement range in the test. Figure 2 shows the calibrating data as follows.

2.2. UCS and Triaxial Compression Test. Uniaxial and triaxial compression tests were performed on 23 circular cylinders, including 14 sandstone specimens and 9 granite specimens. The specimens were prepared with diameters of 30 mm, 50 mm, and 100 mm to evaluate the size dependence of the strength. The loading program was in accordance with ISRM standards and tested within a servo-hydraulic system of TAW-2000. Failure specimens are shown in Figure 2, and the results are listed in Table 1. The number of images is defined as "rock type-size-confining pressure-ID." For example, S3060-0-1 means the first sandstone specimen with 30 mm × 60 mm size and 0 confining pressure.

It can be concluded that the strength of this kind of sandstone would show a deviation between different sizes. When the diameters of specimen change from 30 mm to 100 mm, the uniaxial compression strength increases from 40 MPa to 59.35 MPa. If the size is larger than 50 mm, the UCS changes a little and the trend is the same as the findings of Chen Yu et al. [18], Peng Chen and Zhiwei Zhou [19], and Chuangye Wang and Xiaoya Du [20].

Strength curves of cylindrical sandstone samples with different radiuses are shown in Figure 3. The transition of failure modes can be obtained, and the samples show more ductile feature with the increasing of radial stress. Similarly, a set of tests for chalk were conducted by Ali Tarokh et al. in 2016 [21], and the results showed the transition of failure modes (see Figure 4). Both in sandstone and granite tests, the orientation of the failure planes varies from vertical to horizontal with the increase of mean stress (see Figure 5) which is consistent with the announced results of Tarokh's research.

3. Surface Instability Test

3.1. Instruments and Sample Preparation. The loading equipment used in the test was the TAW-2000 servo rock triaxial testing machine produced by Changchun Chaoyang Test Instrument Co., Ltd. The maximum axial test force is 2000 kN. This test also introduced the VIC-3D system.

The selected test samples are Sichuan yellow sandstones (size: 80 × 90 × 60 mm; sample numbers: S8090110-1, S8090110-2, S8090110-3, S8090110-4, and S8090110-5) and one granite sample (number: 80 × 90 × 60 mm: H809060-1) (see Figure 6). The sample surface was coated with a stearic acid lubricant to reduce friction [22].

3.2. Preparation and Operation of the Surface Instability Simulation Test

3.2.1. Surface Treatment of Rock Samples. The spot image was made by the random seal method. In the test, the speckled surface of the sample needs to contact with the acrylic plate and generate intermediate principal stress, and the coating will increase the thickness of the sample [23]. Therefore, through the steps of surface cleaning-background coating-speckle fabrication-surface lubrication, a relatively clear and distinguishable speckle image with a uniform coating is formed.

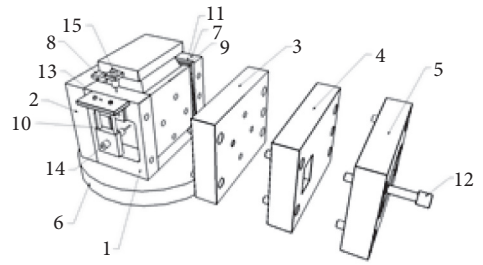

Figure 1: Apparatus for simulation of surface instability. 1: front wall; 2: left wall; 3: perforated wall; 4: half window wall; 5: full-window wall; 6: base; 7: back wall; 8: wedge plate; 9: FRP backing plate; 10: square specimen; 11: ordinary steel base plate; 12: high strength bolt; 13: LVDT holder; 14: holder; 15: top plate.

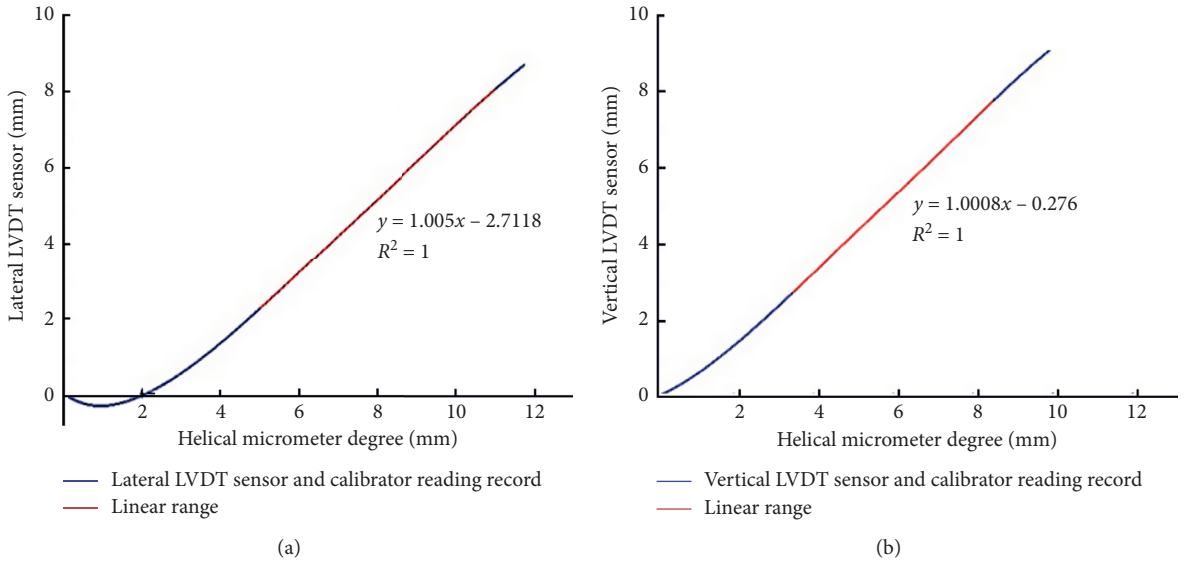

Figure 2: LVDT sensor calibration data. (a) Horizontal LVDT sensor calibration data (red line indicates the linear range). (b) Vertical LVDT sensor calibration data (red line indicates the linear range).

Table 1: Results from compression experiments of sandstone specimens.

Diameter (mm)	Confining pressure (MPa)	Axial stress (MPa)
30	0	40.68
30	0	39.16
30	10	120.01
30	10	126.99
30	20	175.13
30	20	170.87
30	30	210.43
30	30	232.57
50	0	56.37
50	10	140.13
50	20	158.34
50	30	200.96
100	0	59.35

3.2.2. Test Operation Procedure

Step 1. Cyclic preloading and unloading were applied before the test to extrude excessive lubricant and form a uniform membrane, specifically, two cycles were conducted with a preloading start from 0 kN to 100 kN at the rate of 2 kN/s and then unloading to 1 kN.

Step 2. The experiment required to set up the imaging angle and focal length of the camera in VIC-3D system; turn on the VIC-3D system and set the frame rate of the

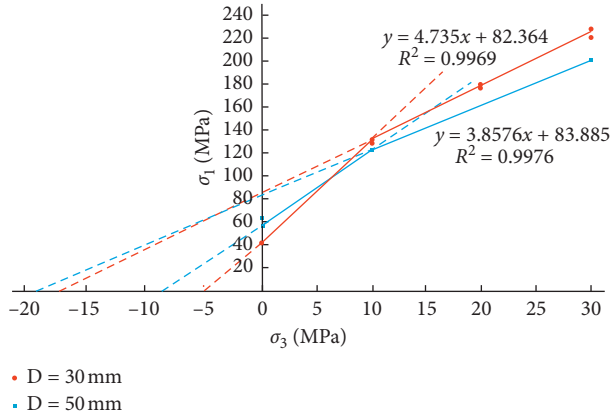

Figure 3: Strength curves of sandstone samples.

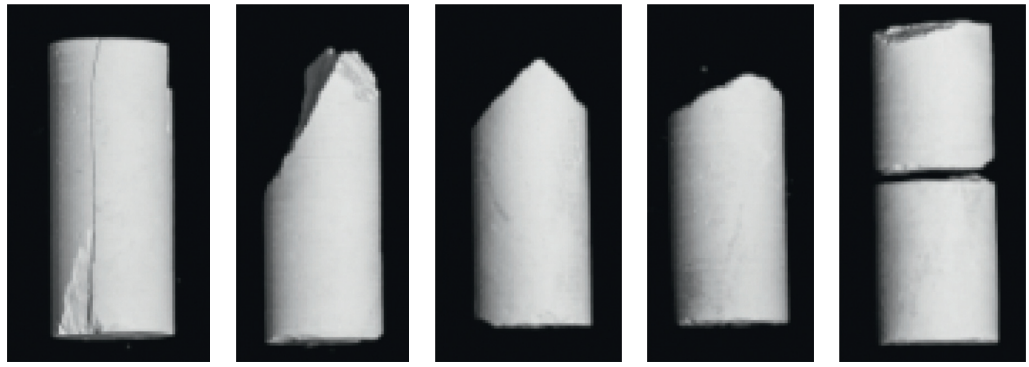

Figure 4: Photographs of failed specimens of Mons chalk. A transition of failure patterns with increase in radial stress. Specimen (a) shows axial splitting observed in uniaxial compression test, $\sigma_3 = 0$; specimen (b) exhibits a shear band with angle of 67° from $\sigma_3 = 1.5$ MPa; specimen (c) also illustrates a shear band with angle of 55° from $\sigma_3 = 2.5$ MPa; specimen (d) shows a transitional failure plane with angle of 36° from $\sigma_3 = 5$ MPa; and stage (e) clearly shows a compaction band under $\sigma_3 = 10$ MPa [21].

image collector to 1 frame/second until the end of the experiment. The destruction simulation experiment is shown in Figure 7.

Step 3. The test loading was divided into two steps: (a) loading to 30% of the uniaxial compressive strength of the sample at 0.5 kN/s load-control rate. (b) The control mode was switched to the transverse LVDT displacement-control at the rate of 0.01 mm/min. The loading proceeded until the failure of the sample and stopped after the occurrence of multiple fractures.

4. Results of the Surface Failure Test

4.1. Fracture Expansion Image of the Specimen. The $80 \times 90 \times 110$ mm cubic sandstone and $80 \times 90 \times 60$ mm cubic granite specimen were loaded, respectively, and the sample results are shown in Figure 8. In Figure 8, the right side of the sample is the free surface. It can be seen from the figure that the failure of the sample in the bidirectional stress state first occurs at the free surface end, mainly near-vertical splitting, and then the cracks extend to the depth. The crack spacing increases as the crack angle increases.

According to the definition of x, y, and z directions as shown in Figure 9, the imaging results (positive as tensile strain and negative as compressive strain) of S8090110-3, S8090110-4, and S8090110-5 in the critical state are shown in Figure 10, and the tensile strains at failure are 2157 $\mu\varepsilon$, 2423 $\mu\varepsilon$, and 2401 $\mu\varepsilon$, respectively.

According to the DIC images, with the increase of the pressure, the deformation of the sample below side of the free face reaches the limit value firstly, and a local vertical crack appears. Afterward, the cracks will not stop developing and expanding along a similar vertical direction until the entire sample is destroyed. By comparing the global strain measured by the LVDT sensor with the local strain of the DIC image, the DIC image would be more suitable for the monitor of local cracks development.

4.2. Loading-Displacement Analysis of Rock Samples

4.2.1. Sandstone. The test results of the vertical stress-vertical strain curve and the test results of the vertical stress-transverse strain curve of cubic sandstone under test loading are shown in Figure 11. It can be found that

Figure 5: Crack image of failed specimens. (a) Sandstone specimens. (b) Granite specimens.

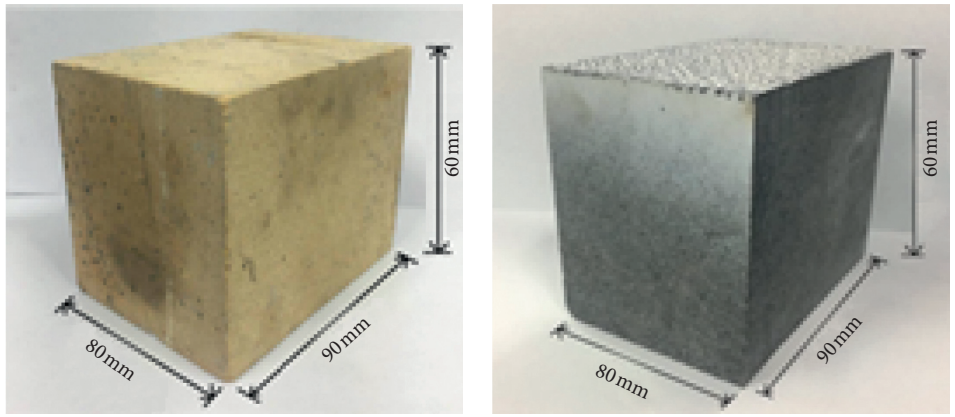

Figure 6: Rock samples. (a) Sandstone sample. (b) Granite sample.

the failure of sandstone samples occurred when the transverse strain reached 2000 $\mu\varepsilon$. The strength will continue to fluctuate after the first cracking, even exceeding the first cracking strength. The first failure strength of the sample (almost 60 MPa) is consistent with the UCS (59.35 MPa for 100 mm size specimen; see Table 1) of the same stone sample, indicating that the shape of the sample does not influence its strength.

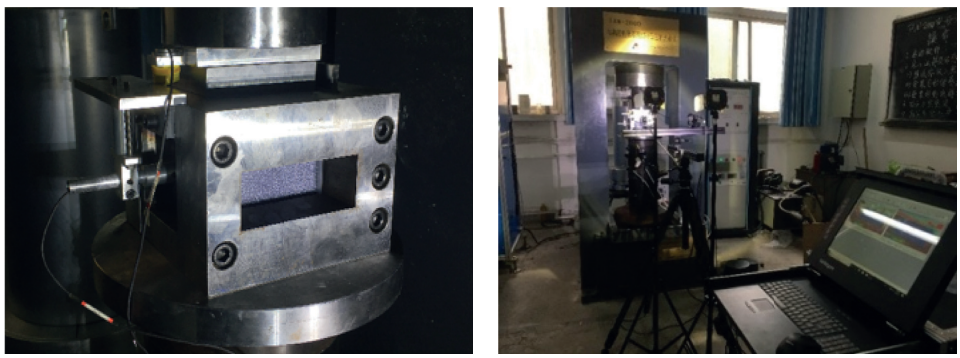

(a) (b)

Figure 7: Test systems. (a) Rock wall chamber. (b) Damage measurement process.

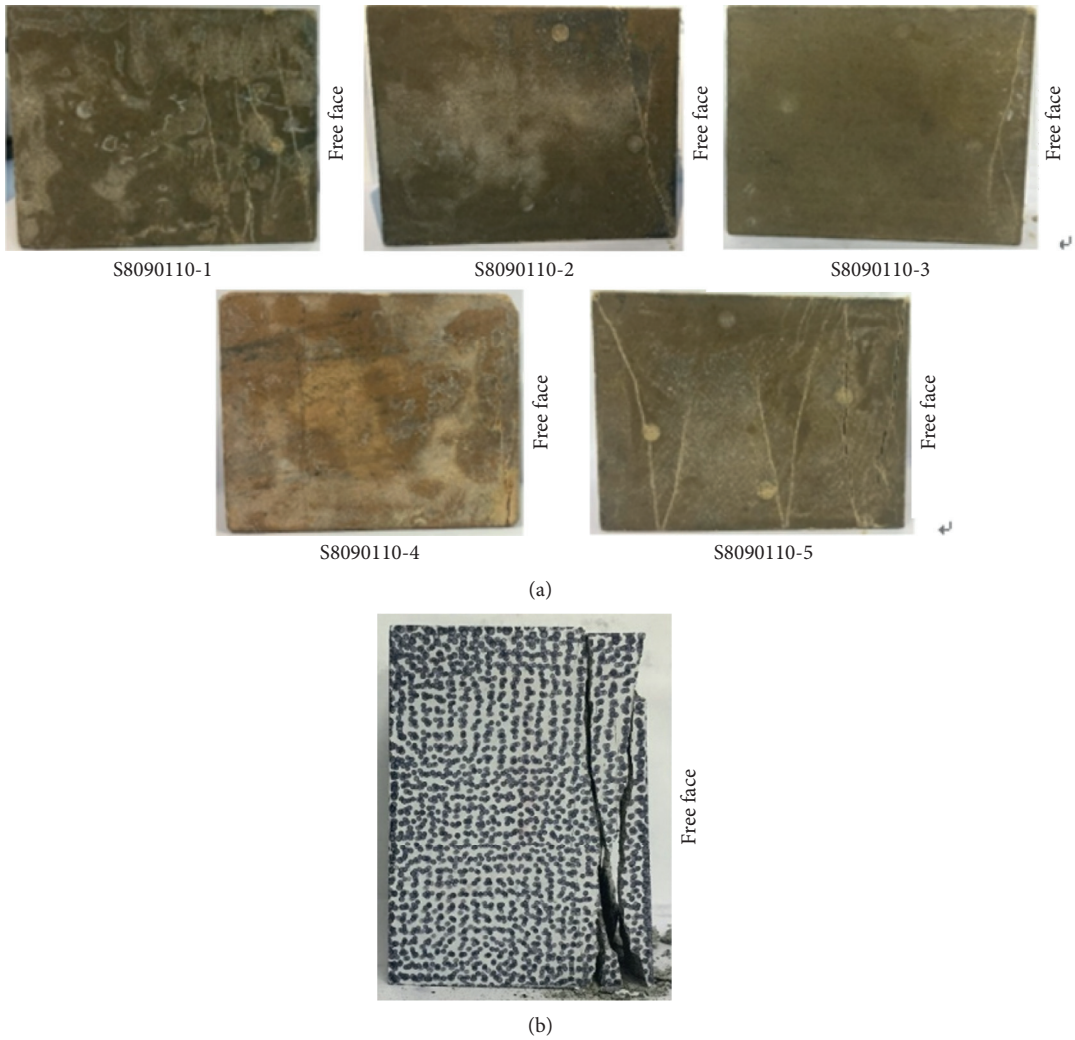

Figure 8: Damage images of samples. (a) Sandstone damage results. (b) Granite damage results.

4.2.2. Granite. The results of the vertical stress-vertical strain curve and the vertical stress-transverse strain curve of cubic granite are shown in Figure 12. It can be found that the failure of granite samples occurred when the transverse strain reached 4500. The strength will increase again after the first cracking, even exceeding the first cracking strength.

4.3. Analysis of Transitional Failure Mode. Failure of rock is a complex process and failure mechanisms which would show a transition feature according to stress level and loading condition [24, 25]. Previous research proposed that an increase in effective pressure shifts the macroscopic failure mode from brittle to ductile [26]. According to the difference

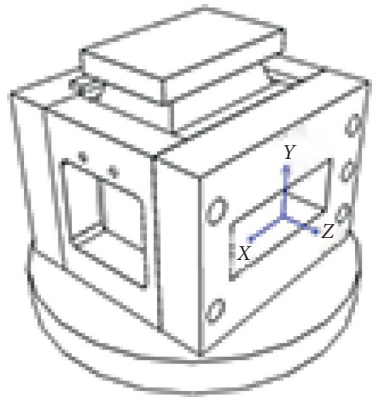

Figure 9: VIC-3D system direction definition.

of microcracks propagation, Charles Derek Martin [27] divided the stress-strain curves of brittle rock into five regions, which represent the process of microcracks propagation, and indicated that the initial step in the failure process is sliding along grain boundaries, with the wing or axial cracks developing much later in the failure process. The transition of failure modes will cause the change of the orientation of the failure plane, which decreases from 90° to 0° with the increase in mean stress [21]. From the analysis of fracture angle, cracks spacing, failure location, and stress-strain relationship curves shown in Figures 8–12, it can be seen that the first fracture of the samples occurs close to the free surface, which could be thought as a type of tensile failure. As the pressure continually rises, shear failure appears and a sliding surface can be found in deeper location of samples. After the fractures are fully developed, it can be found that the transitional failure mode from tensile failure to shear failure occurs from the free face to the depth, which simulates the stress and strain characteristics of the rock in the biaxial stress state and reproduces the stress state of the tunnel rock wall. In the uniaxial and triaxial tests in the laboratory, the failure mode of the sample is a combination of tensile and shear failure, while the first failure of the rock in the surface instability chamber is in tensile failure mechanism; however, the failure mode has gradually transformed to shear mode as the increase of the failure depth.

5. Research of Tunnel Wall Strength Based on the Maximum Principal Strain Theory

Under uniaxial compression or biaxial loading, the failure mode of the sample is mainly tensile failure rather than shear failure at first, so the strength is different from the value predicted by the Mohr–Coulomb criterion. In explaining these destruction phenomena, many scholars have put forward different viewpoints. Martin proposed the CWFS model [28] and emphasized that damage development caused that as friction was mobilized in the sample and led to the reduction of cohesion [29]. Martino and Chandler thought that the damage zone where the stress redistribution happened was too small to permanently change rock properties [30]. Brace and Gramberg have first provided explanations on the tensile crack under uniaxial compression condition [31, 32] that is because the tensile strain is caused by tensile damage. Stacey attempted to use the theory of maximum principal strain to forecast the brittle failure mechanism of deep massive quartzite in South Africa; he suggested that for those materials with obvious linear deformation behaviors, the failure could be considered to relate to the tensile strain [15].

Since the failure mode of the surrounding rock is tensile failure, it cannot be explained by the Mohr–Coulomb criterion. Based on the maximum principal strain theory proposed by Stacey and Nick Barton and generalized Hooke's law, the following failure conditions can be obtained:

$$\begin{cases} \varepsilon_1 \text{ or } \quad \varepsilon_2 \text{ or } \quad \varepsilon_3 = \varepsilon_c, \\ \varepsilon_3 = \dfrac{1}{E}\left[\sigma_3 - \mu\left(\sigma_1 + \sigma_2\right)\right], \\ \varepsilon_2 = \dfrac{1}{E}\left[\sigma_2 - \mu\left(\sigma_1 + \sigma_3\right)\right], \\ \varepsilon_1 = \dfrac{1}{E}\left[\sigma_1 - \mu\left(\sigma_2 + \sigma_3\right)\right], \end{cases} \tag{1}$$

where E is the elastic modulus, μ is Poisson's ratio value, $\sigma_{1,2,3}$ stands for principal stresses, and $\varepsilon_{1,2,3}$ means principal strains. If the calculated extensional strain was greater than the critical strain, then spalling would occur. So, if $\mu\left(\sigma_1 + \sigma_2\right) > \sigma_3$, then (negative) extensional strain will occur.

According to the generalized Hooke's law,

$$\sigma_2 = \mu\left(\sigma_1 + \sigma_3\right). \tag{2}$$

By iterative substitution of equation (2) in (1), the following can be obtained:

$$\varepsilon_1 = \frac{1}{E}\left[\left(1 - \mu^2\right)\sigma_3 - \mu\left(1 + \mu\right)\sigma_1\right]. \tag{3}$$

Therefore, a simplified maximum principal strain theory equation can be obtained:

$$\sigma_1 = \frac{1 - \mu}{\mu}\sigma_3 - \frac{E\varepsilon_c}{\mu\left(1 + \mu\right)}, \quad \left(\text{when} \quad \varepsilon_c < 0\right). \tag{4}$$

In the test, the minimum principal stress is 0 for free face, and equation (4) yields

$$\sigma_1 = -\frac{E\varepsilon_c}{\mu\left(1 + \mu\right)}. \tag{5}$$

Elastic modulus, E, and Poisson's ratio, μ, can be calculated according to the UCS test. The parameters of sandstone samples are 7.07 GPa and 0.24, respectively. From equation (5), the critical principal strain ε_c can be given as -2.526×10^{-3} (negative value means tensile strain). Initial fracture creates strain values measured from LVDT sensor and DIC image (the measured value is 2300 and 2400, respectively) which are consistent with ε_c, so it can be considered that the initial failure mode of sandstone samples is a tensile failure and the maximum principal strain theory has good applicability to explain the surface failure of the rock wall.

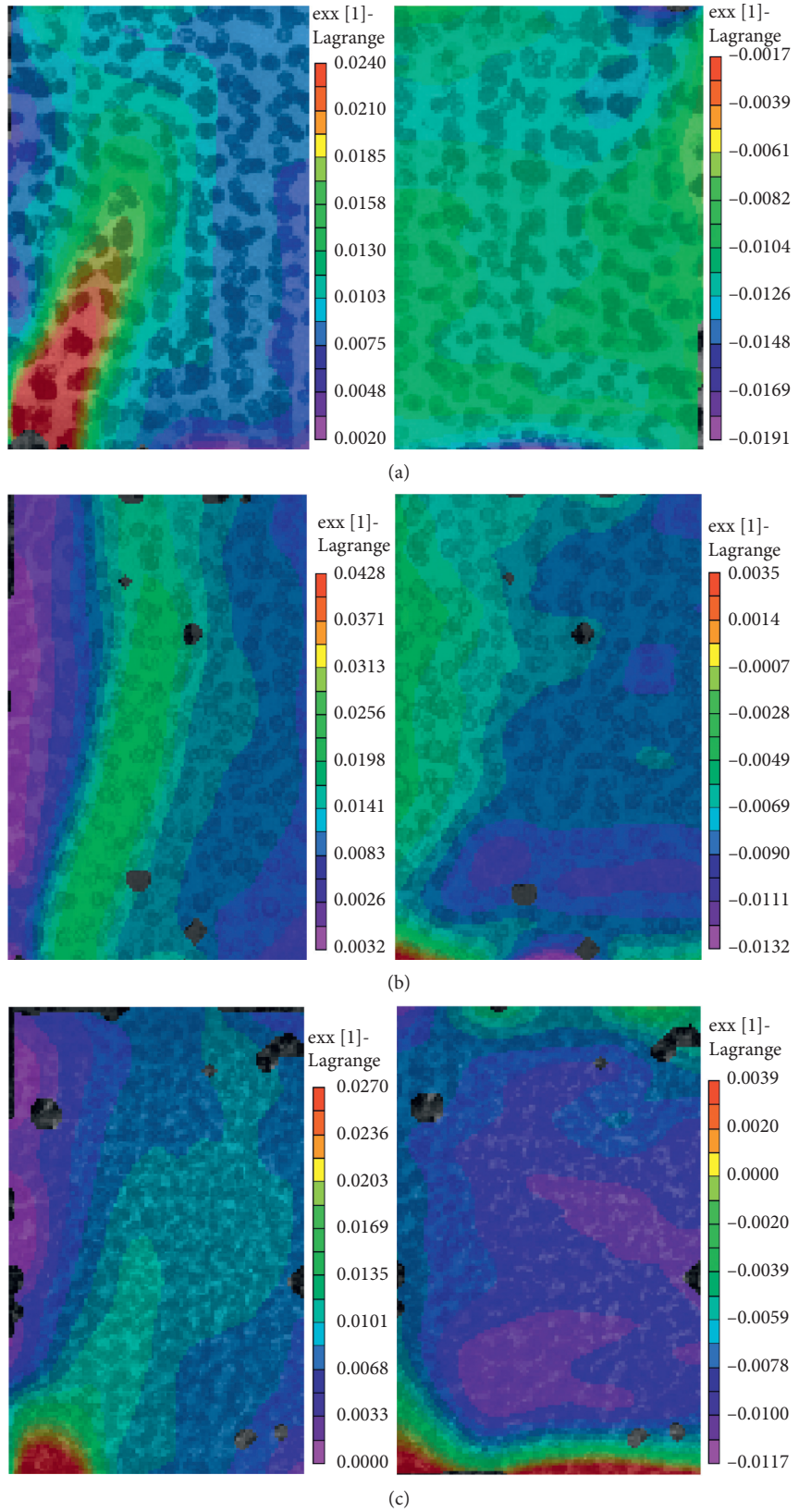

Figure 10: Imaging results when DIC processes critical damage (positive as tensile strain, negative as compressive strain). (a) S8090110-3 critical strain DIC map (unit: cm): (left) X-direction displacement field and (right) Y-direction displacement field. (b) S8090110-4 critical strain DIC map (unit: cm): (left) X-direction displacement field and (right) Y-direction displacement field. (c) S8090110-5 critical strain DIC map (unit: cm): (left) X-direction displacement field and (right) Y-direction displacement field.

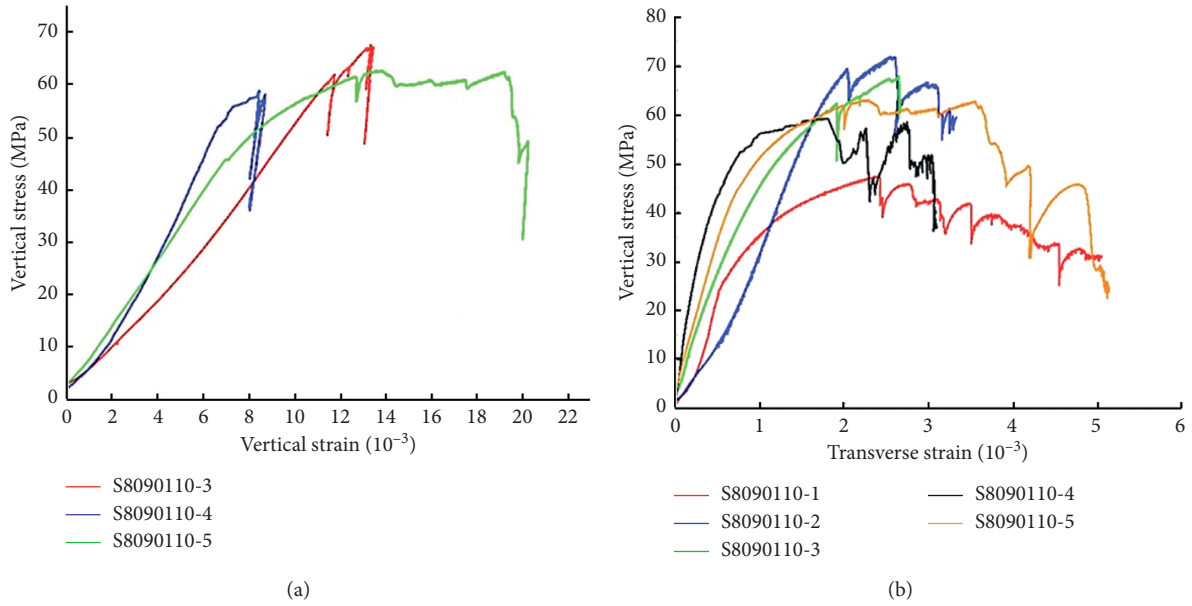

Figure 11: Stress versus strain curves of the cubic sandstone samples. (a) Vertical stress-vertical strain curve of the sandstone sample. (b) Vertical stress-transverse strain curve of the sandstone sample.

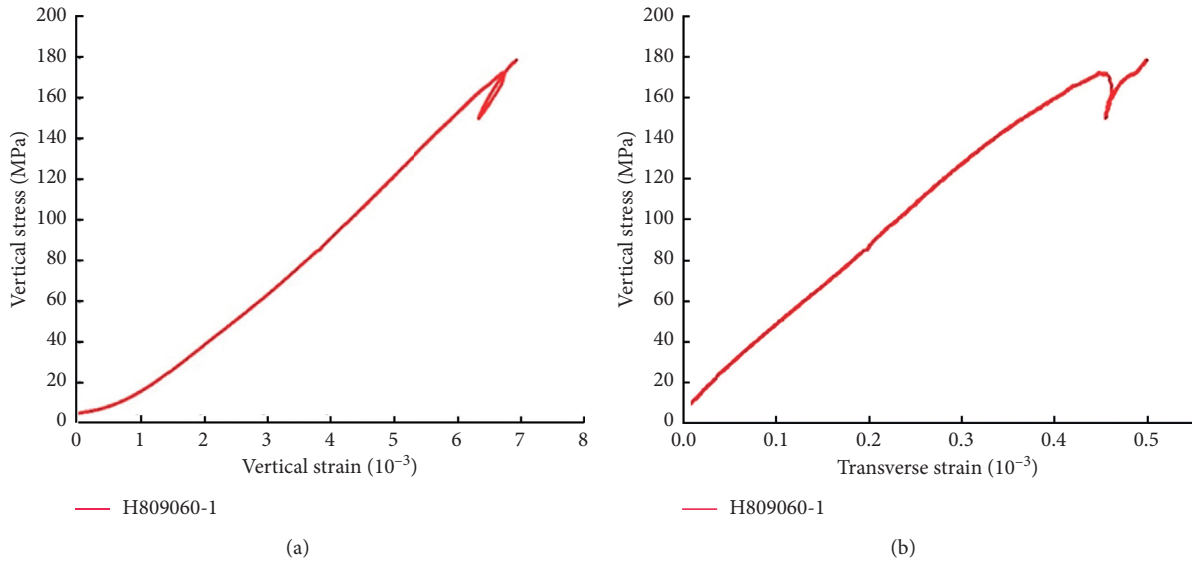

Figure 12: Stress versus strain curves of the cubic granite samples. (a) Vertical stress-vertical strain curve of the granite sample. (b) Vertical stress-strain curve of the granite sample.

Since the failure of the sample is not only shear failure in the uniaxial case, the strength value of the rock is higher in the uniaxial case when the Mohr–Coulomb criterion is used to predict it (see Figure 13). However, considering the plane strain problem under biaxial loading, especially the strength feature of the rock wall because the specimen failure is caused by tensile failure, the maximum principal strain theory is more in line with the actual situation (see Figure 13).

The maximum principal strain theory can also be suitable for the calculation of uniaxial compression strength when the stretching lineation strain failure takes place (see Figures 3 and 8). Li Yuan et al. proposed a brittle-shear mixing strength criterion and considered rock failure as brittle fracture and shear failure [33]. The coefficient b was proposed to describe the transition from brittle failure to a shear failure caused by constant confining pressure; see the following:

$$\sigma_1 = b\left(C_1\sigma_3 + C_2\right) + (1-b)\left(D_1\sigma_3 + D_2\right), \quad (6)$$

$$b = e^{m\sigma_3+n}, \quad (7)$$

where $(C_1\sigma_3 + C_2)$ represents the brittle fracture strength; $(D_1\sigma_3 + D_2)$ is the shear strength; C_1, C_2, D_1, and D_2 are the material strength coefficients obtained by the experiments; b

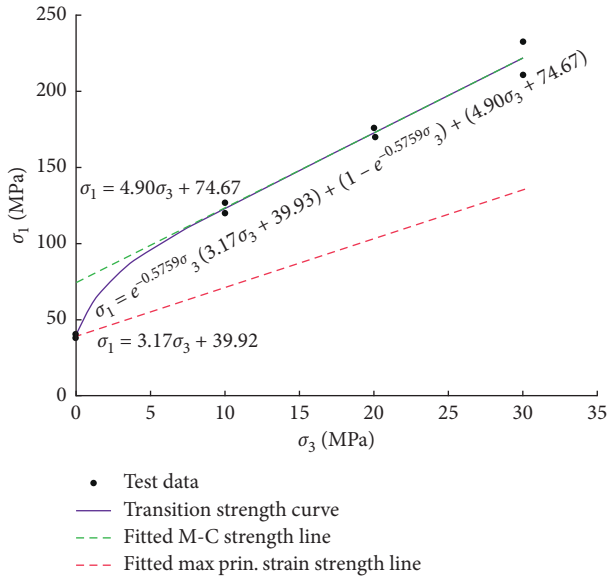

Figure 13: Comparison of three strength theories.

Table 2: Parameters fitted and calculated from data of specimen with 30 mm diameter.

Parameter	E (GPa)	μ	C_1	C_2 (MPa)	D_1	D_2 (MPa)	m (MPa^{-1})	n	R
Value	7.07	0.24	3.17	39.92	4.90	74.67	−0.5759	0	0.9961

indicates the transition coefficient from brittle failure to shear failure ranging from 0 to 1; m and n are parameters fitted out by data.

If equation (6) is used to explain the transitioning of failure mode with the stress state changing, the results are shown in Figure 13. Mohr–Coulomb strength line could be fitted by the higher stresses data and the maximum principal strain strength line could be calculated by E, μ, and UCS of 30 mm size sample mentioned in Table 2. But, according to the test condition of the uniaxial and triaxial compression test, equation (2) should be changed to

$$\sigma_2 = \sigma_3. \tag{8}$$

The deductive program is the same as equations (3) to (5); it can be given that

$$\sigma_1 = \frac{1-\mu}{\mu}\sigma_3 - \frac{E\varepsilon_c}{\mu}, \quad (\varepsilon_c < 0). \tag{9}$$

Because the average UCS value is 39.92 MPa, the related critical strain can be calculated by equation (9) as -1355×10^{-3}. The strength line of ε_c is illustrated in Figure 13 as the red line. Equation (6) is fitted by the test data shown in Figure 13. C1 and C2 are confirmed by slope and intercept of equation (9) and D1 and D2 by the parameters of Mohr–Coulomb strength theory which is fitted in Figure 13. Fitted and calculated parameters are given in Table 2, and the correlation coefficient arrives at 0.9961.

The test data and transition trend of sandstone samples can further illustrate the reason why the in situ strength of tunnel wall is lower than the predicted strength value by Mohr–Coulomb theory; that is, the tensile failure is not considered, which leads to a higher predicted strength value.

6. Conclusion

Experimental study of surface instability of samples was carried out. An indoor test device for the simulation of transitional surface failure of the rock wall was developed. Through a biaxial stress loading test on the rectangular rock sample, the damage process and crack development of rock samples were analyzed and the law of stress and strain related to the failure mode transition was characterized as well. The following conclusions can be deducted:

(1) The surface fracture of the rock wall is a transitional failure mode. It is found in the simulation test that, under the condition of biaxial loading, with the continuous rise of pressure, the crack caused by tensile failure first appears at the end of the free surface and followed by shear failure. The experiment simulates the stress-strain characteristics under the in situ stress state of the rock wall. This phenomenon is also applicable to granite, and it is concluded that tensile failure is the main reason why the wall strength of both shallow and deep tunnel is lower than indoor strength.

(2) The maximum principal strain theory is applied to explain the tensile failure of samples. Under the condition of biaxial stress, the maximum principal strain theory was deduced. Additionally, test data were used

to verify the correctness of the maximum principal strain theory to explain the tensile failure of the sample.

(3) Transitional failure mode leads to the conversion of strength criterion. Considering the transitional failure mode of the rock wall, the surface fracture needs to refer to the theory of maximum principal strain. As the failure gradually evolved to the depth, the mode changes from tensile failure to shear failure. The theory of maximum principal strain may no longer be applicable, and Mohr–Coulomb criterion or other failure criteria are acceptable.

Data Availability

The data used to support the findings of this study are included within the article.

Conflicts of Interest

The authors declare that there are no conflicts of interest regarding the publication of this paper.

Acknowledgments

Dr. N.F. Deng is acknowledged for his comprehensive treatment of the literature. This research was funded by the National Key R&D Program of China (no. 2018YFE0101100).

References

[1] G. Su, T. Li, and J. Jiang, "Experimental study of influence of support failures on rockbursts under true-triaxial condition," *Advances in Civil Engineering*, vol. 2018, Article ID 2105451, 20 pages, 2018.

[2] J. Pan, S. Liu, and S. Wang, "A new theoretical view of rockburst and its engineering application," *Advances in Civil Engineering*, vol. 2018, Article ID 4683457, 12 pages, 2018.

[3] Q. Jiang, X.-T. Feng, T.-B. Xiang, and G.-S. Su, "Rockburst characteristics and numerical simulation based on a new energy index: a case study of a tunnel at 2,500 m depth," *Bulletin of Engineering Geology and the Environment*, vol. 69, no. 3, pp. 381–388, 2010.

[4] F. Pei, H. Ji, and J. Zhao, "Energy evolution and AE failure precursory characteristics of rocks with different rockburst proneness," *Advances in Civil Engineering*, vol. 2020, Article ID 8877901, 12 pages, 2020.

[5] X. Sun, Li Gan, and C. Zhao, "Numerical investigation of gob-side entry retaining through precut overhanging hard roof to control rockburst," *Advances in Civil Engineering*, vol. 2018, Article ID 8685427, 10 pages, 2018.

[6] W. F. Brace and E. G. Bombolakis, "A note on brittle crack growth in compression," *Journal of Geophysical Research*, vol. 68, no. 12, pp. 3709–3713, 1963.

[7] M. S. Paterson, "Experimental deformation and faulting in wombeyan marble," *Geological Society of America Bulletin*, vol. 69, no. 4, pp. 465–467, 1958.

[8] Z. Lian, L. Tian, and W. Wang, *Brown Waits for Underground Rock Engineering*, Metallurgical Industry Press, Beijing, China, 1986.

[9] E. Hoek and C. D. Martin, "Fracture initiation and propagation in intact rock-a review," *Journal of Rock Mechanics and Geotechnical Engineering*, vol. 6, no. 4, pp. 287–300, 2014.

[10] J. P. Meyer and J. F. Labuz, "Linear failure criteria with three principal stresses," *International Journal of Rock Mechanics & Mining Sciences*, vol. 12, no. 40, p. 180, 2012.

[11] B. G. Tarasov and M. F. Randolph, "Frictionless shear at great depth and other paradoxes of hard rocks," *International Journal of Rock Mechanics and Mining Sciences*, vol. 6, no. 1, pp. 316–328, 2017.

[12] V. V. Makarov, M. A. Guzev, V. N. Odintsev, and L. S. Ksendzenko, "Periodical zonal character of damage near the openings in highly-stressed rock mass conditions," *Journal of Rock Mechanics and Geotechnical Engineering*, vol. 8, no. 2, pp. 164–169, 2016.

[13] X. Fan, K. Li, and H. Lai, "Experimental and numerical study of the failure behavior of intermittent rock joints subjected to direct shear load," *Advances in Civil Engineering*, vol. 2018, Article ID 4294501, 19 pages, 2018.

[14] N. Barton and B. Shen, "Risk of shear failure and extensional failure around over-stressed excavations in brittle rock," *Journal of Rock Mechanics and Geotechnical Engineering*, vol. 9, no. 2, pp. 210–225, 2017.

[15] T. R. Stacey, "A simple extension strain criterion for fracture of brittle rock," *International Journal of Rock Mechanics and Mining Sciences & Geomechanics Abstracts*, vol. 18, no. 6, pp. 469–474, 1981.

[16] C. S. Kao, *Surface instability as damage evolution in rock*, Ph.D. dissertation, University of Minnesota, Minneapolis, MN, USA, 2011.

[17] Z. Li, L. Wang, and Y. Lu, "Experimental investigation on the deformation, strength, and acoustic emission characteristics of sandstone under true triaxial compression," *Journal of Mining and Safety Engineering*, vol. 36, no. 1, pp. 191–197, 2019.

[18] Yu Chen, Y.-heng Huang, and P. Cao, "Size effect experimental study of strength and deformation in different height-to-diameter ratio soft rocks," *Journal of Central South University*, vol. 41, no. 3, pp. 1073–1078, 2010.

[19] P. Chen and Z. Zhou, "Size effect experiment of rock material with RFRA^{2D}," *Journal of Liaoning Technical University (Natural Science)*, vol. 31, no. 6, pp. 842–845, 2012.

[20] C. Wang and X. Du, "Comparative analysis of rock size effect test and RFPA^{3D} numerical simulation," *Industrial Minerals & Processing*, vol. 47, no. 2, pp. 28–30, 2018.

[21] T. Ali, L. Yuan, and J. F. Labuz, "Hardening in porous chalk from precompaction," *Acta Geotechnica: An International Journal for Geoengineering*, vol. 12, pp. 949–953, 2017.

[22] Y. Peng, Q. Guo, Z. Zhang, and Y. Shan, "Application of base force element method on complementary energy principle to rock mechanics problems," *Mathematical Problems in Engineering*, vol. 2015, Article ID 292809, 16 pages, 2015.

[23] Y. Zheng and S. Deng, "Failure probability model considering the effect of intermediate principal stress on rock strength," *Mathematical Problems in Engineering*, vol. 2015, Article ID 960973, 7 pages, 2015.

[24] Q. Jiang, G. Su, X.-T. Feng, G. Chen, M.-Z. Zhang, and C. Liu, "Excavation optimization and stability analysis for large underground caverns under high geostress: a case study of the Chinese laxiwa project," *Rock Mechanics and Rock Engineering*, vol. 52, no. 3, pp. 895–915, 2019.

[25] Q. Jiang, B. Yang, and F. Yan, "New method for characterizing the shear damage of natural rock joint based on 3D engraving

and 3D scanning," *International Journal of Geomechanics*, vol. 20, no. 2, Article ID 6019022, 2020.

[26] T.-F. Wong, H. Szeto, and J. Zhang, "Effect of loading path and porosity on the failure mode of porous rocks," *Applied Mechanics Reviews*, vol. 45, no. 8, pp. 281–293, 1992.

[27] M. Charles Derek, *The Strength of Massive Lac Du Bonnet Granite Around Underground Openings*, Winnipeg Manitoba: Department of Civil & Geological Engineering University of Manitoba, Winnipeg, Canada, 1993.

[28] C. D. Martin, "Seventeenth Canadian geotechnical colloquium: the effect of cohesion loss and stress path on brittle rock strength," *Canadian Geotechnical Journal*, vol. 34, no. 5, pp. 698–725, 1997.

[29] C. D. Martin and N. A. Chandler, "The progressive fracture of lac du bonnet granite," *International Journal of Rock Mechanics and Mining Sciences & Geomechanics Abstracts*, vol. 31, no. 6, pp. 643–659, 1994.

[30] J. B. Martino and N. A. Chandler, "Excavation-induced damage studies at the underground research laboratory," *International Journal of Rock Mechanics and Mining Sciences*, vol. 9, no. 10, pp. 1413–1426, 2004.

[31] W. F. Brace, "Recent experimental studies of brittle fracture of rocks," in *Proceedings of the 10th US Symposium on Rock Mechanics*, American Rock Mechanics Association, Austin, TX, USA, pp. 58–81, May 1966.

[32] J. Gramberg, "The axial cleavage fracture 1 axial cleavage fracturing, a significant process in mining and geology," *Engineering Geology*, vol. 1, no. 1, pp. 31–72, 1965.

[33] Li Yuan, Z. Yan, and Q. Li, "Strength analysis of rock materials under brittle shear failure mode," *Journal of University of Science and Technology Beijing*, vol. 12, no. 19, pp. 1364–1370, 2012.